FLOW CHARACTERISTICS OF A HELICOPTER FUSELAGE CONFIGURATION INCLUDING A ROTATING ROTOR HEAD

Moritz Grawunder, Roman Reß, Christian Breitsamter, Nikolaus A. Adams
Institute of Aerodynamics and Fluid Mechanics, Technische Universität München
moritz.grawunder@aer.mw.tum.de

Keywords: *helicopter, blunt body wake, drag breakdown*

Abstract

*The reduction of emissions in air transport is clearly a main goal of the aeronautical industry today, addressing both fixed wing aircraft and rotorcraft. The first phase of the **ADHeRo** (**A**erodynamic **D**esign Optimization of a Helicopter Fuselage including a Rotating Rotor Head) project contributed to achieving this goal by providing detailed flow characteristics and drag analysis of a state-of-the-art Twin Engine Light class utility helicopter. This was achieved by means of wind tunnel experiments and numerical simulations.*
It has been shown that optimizing the parasite drag of such a configuration is a vital approach for achieving efficiency gains. In particular, this can be obtained by reducing the drag of the rotor head, the landing skids and the fuselage. The analysis revealed that reducing the interference drag of the landing skids and the rotor head on the fuselage also provides significant potential for efficiency gains. On the other hand, the analysis showed the importance of considering changes in the lift characteristics when optimizing components. Otherwise, efficiency gains could be lost due to higher power requirements for the main rotor.

Symbols

A_{ref}	Reference area	[m^2]
C_D,C_Y,C_L	Drag, side force and lift coefficient	[-]
F_D,F_Y,F_L	Drag, side force and lift	[N]
h_0	Height of prism cells at the wall	[m]
$l_{x,ref}$	Reference length in x-direction	[m]
P	Power	[W]
U_∞	Freestream velocity	[m / s]
y^+	Dimensionless wall distance	[-]
Ψ	Rotor head azimuth angle	[deg]
α	Angle of attack	[deg]
β	Angle of side slip	[deg]
ρ	Fluid density	[kg / m^3]
ω_x	Axial vorticity	[1 / s]

1 Introduction

To speed up the progress in reducing emissions in air transport, the European Commission together with the European Aeronautical Industry launched the CleanSky program. Under CleanSky, environmental issues in the rotorcraft domain are addressed by the Green Rotorcraft Consortium (GRC). Even though fixed-wing aircraft generally outperform rotorcraft in terms of fuel efficiency, range, speed and noise, rotorcraft are still of high importance. The reason for this is their unique Vertical Take-Off and Landing (VTOL) capability. Thus measures are taken by the GRC to reduce emissions and to increase the fuel efficiency and productivity of rotorcraft. The GRC subproject **AD**HeRo (**A**erodynamic **D**esign Optimization of a Helicopter Fuselage including a Rotating Rotor Head) contributes to achieving this goal by aiming to reduce parasite drag for Twin Engine Light (TEL) - class utility helicopters in fast level flight without increasing the fuselage down force.
TEL-class helicopters play an important role in today's air services. The TEL-class includes helicopters with a Maximum Take of Weight (MTOW) below 4 metric tons and with two engines installed. The missions performed by this helicopter class include Helicopter Emergency Medical Services (HEMS), Search and Rescue (SAR) missions, law enforcement,

offshore supply (oil & gas, wind farms) and executive transport.

In the helicopter fleet from the year 2000, the TEL-class accounted for approximately 10% of the global flight hours performed by civil helicopters [1]. Thus improving the efficiency in the TEL-class can have a relevant impact on the ecological foot print of the global helicopter fleet. For this reason, a state-of-the-art TEL utility helicopter with a bearingless main rotor system is subject to the optimization performed through **AD**HeRo.

To assess viable approaches for improving the efficiency of a helicopter, the breakdown of the total power requirements can be indicative. According to Stroub and Rabbott [2], the total power requirements P_{TOT} for a helicopter in forward level flight are defined by the induced power P_i, profile power P_o, parasite power P_p and tail rotor power P_{TR} (single-rotor design).

$$P_{TOT} = P_i + P_o + P_p + P_{TR} \qquad (1)$$

Stroub and Rabbott present values for each of the power fractions for helicopters characterized by 1.4 and 4.5 metric tons MTOW in level flight at 185 km/h; see table 1.

MTOW	P_i	P_o	P_p	P_{TR}
1.4 metric tons	11 %	29 %	55 %	5 %
4.5 metric tons	21 %	33 %	41 %	5 %

Table 1. Power breakdown in percentage of total power of two helicopters with 1.4 and 4.5 metric tons MTOW in level flight (185 km/h), taken from [2].

From table 1 it becomes evident that the biggest contributor to the total power requirements in cruise, for helicopters within the envelope of the TEL-class, is the parasite power with some 50 %. The parasite power is the amount of power required to compensate the losses due to the existence of parasite drag. This drag is defined as the force F_D which is generated at non-lifting components of an aircraft and directed opposite to the direction of flight. Thus aiming to reduce parasite drag is a promising approach for increasing the efficiency of TEL-class helicopters.

In order to identify the biggest contributors, the parasite drag breakdown is assessed based on the literature; see Fig. 1.

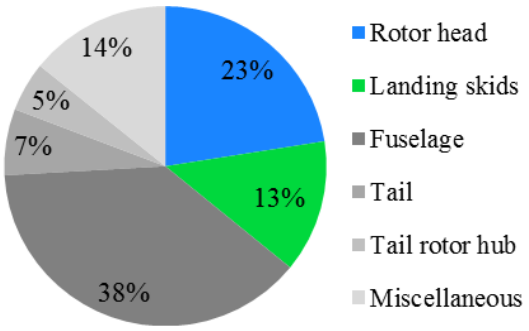

Fig. 1. Parasite drag breakdown in percentage of total parasite drag for a TEL-class utility helicopter in level flight (cruising condition), 2.5 metric tons MTOW [3].

The parasite drag fractions given in Fig. 1 reveal that the three biggest contributors are the rotor head, the landing skids and the fuselage. Together they account for 74 % of the total parasite drag.

$$P_p = F_D\, U_\infty = \tfrac{1}{2}\, \rho\, A\, C_D\, U_\infty^3 \qquad (2)$$

Eq. (2) shows the connection between parasite drag and the power required to compensate this form of drag. This relationship shows that a reduction in parasite drag is linearly transferred to a reduction of parasite power.

For the investigated class of helicopters a 10 % reduction of parasite drag would result in a 5 % reduction of total power requirements in level flight. Thus, optimizing the rotor head, the fuselage and the landing skids with respect to drag is a vital approach in order to achieve efficiency gains. However, this is only true if the down force of the modified components is not increased by optimizing their design with respect to drag. If this is not the case the increase in required rotor power (to compensate the additional down force) could deteriorate the achieved efficiency gains. In consequence the optimization planned within **AD**HeRo has to account for both aspects by aiming to reduce the parasite drag of the fuselage, the landing skids and the rotor head without increasing the down force of the non-lifting components of the aircraft. The planned optimizations are evaluated through extensive Wind Tunnel (W/T) experiments. The experimental investigations are supplemented by performing numerical simulations based on the Reynolds Averaged Navier Stokes (RANS) equation model.

In order to assess the benefits of the planned design modifications, the baseline configuration is analyzed first. Then modifications to the three components of interest are introduced and evaluated against the baseline.
This paper reports on the baseline configuration campaign. This includes configuration studies for both global and local flow parameter based on experimental and numerical results.

2 Model Geometry and Configurations

The full-scale geometry, which is to be reproduced using the **AD**HeRo W/T model, represents a characteristic state-of-the-art TEL utility helicopter with a MTOW of 2.95 metric tons. It features a five-bladed bearingless rotor and a backdoor at the rear fuselage upsweep which is typical for a utility helicopter.
Fig. 3 a) depicts the **AD**HeRo W/T model in its full configuration. The design of the W/T model is primarily driven by the requirement of drag force prediction due to flow separation at the fuselage, landing skids and rotor head. To ensure this, four aspects are essential. First of all, the relevant components of the full-scale geometry have to be reproduced precisely. Second, the aerodynamic interference of the model support and the model itself needs to be minimal. Third, the model scale should be as large as possible. Finally, the rotation of the rotor head and the collective and cyclic pitch motion of the blade cuffs need to be modeled.
The first fact is accounted for in the baseline model design by including the baseline fuselage (F0), mast fairing (M0), landing skid (L0) and rotor head (R0). All of the components resemble their full-scale counterparts precisely except for some necessary simplifications to confine the experimental effort. These simplifications include

- eliminating the flow through the engine canopy and the engine itself by aerodynamically fairing the air intake and closing the ejectors,
- truncating the tail boom at a position just upstream of the tail surfaces and
- truncating the blade cuffs at the first aerodynamic section of the blade.

The model support attached through the tail boom is an in house development by Vogel et al. [4]. This model support nearly eliminates the aerodynamic interference between the support and the model observed with other support designs (bottom or top sting). This results in a more realistic flow topology especially on the rear part of the model, thus allowing precise drag prediction.
In order to achieve the maximum possible model scale, the tail boom is truncated. For the chosen experimental setup, the model scale is mainly limited through the maximum acceptable moment acting on the employed six-component under-floor W/T balance and the elastostatic stability of the support. Without the truncation of the tailboom, the lever arm of the support would be extended by the length of the rear control surfaces. In consequence, the W/T model would have to be of a smaller scale to avoid exceeding the measurement range of the W/T balance and the stability constraints of the support. Exploiting the maximum feasible scale for the chosen experimental setup through an iterative work methodology leads to the final W/T model scale of 1 : 5.
Fig. 2 depicts the design of the W/T model rotor head in detail. As for the other model components, the full-scale geometry is precisely reproduced on all components exposed to the flow. The model rotor head allows for collective and cyclic pitch motion of the blade cuffs through the application of a fully functional swash blade. The swash blade attitude is fixed at a position that represents the trimmed attitude for the full-scale configuration in level flight.

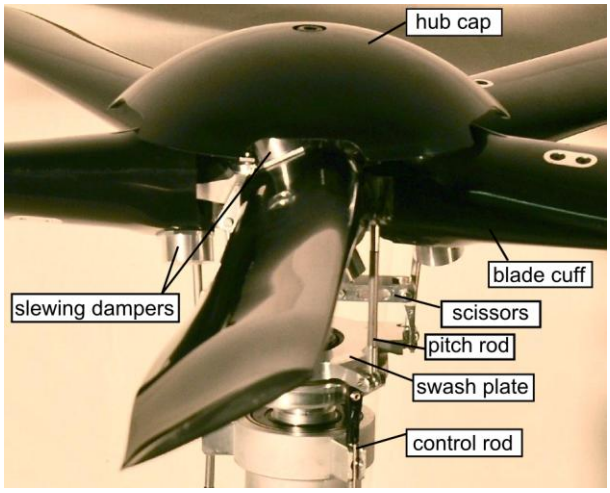

Fig. 2. Detail view of the model rotor head components.

In order to isolate the impact of the cyclic pitch motion of the blade cuffs and to facilitate the comparison with numerical simulations, the

collective pitch input is omitted for some experiments.

a) Fuselage with landing skid and rotor head (F0M0L0R0)

b) Fuselage with rotor head (F0M0R0)

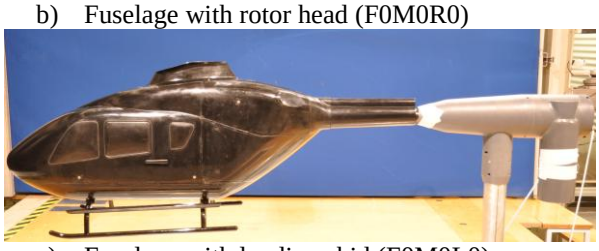

c) Fuselage with landing skid (F0M0L0)

d) Isolated fuselage configuration (F0M0)

Fig. 3. Investigated configurations of the **AD**HeRo wind tunnel model.

Fig. 3 a) to d) show the four different sub-configurations investigated. The analysis of the sub configurations is necessary for studying interference effects between the different components.

3 W/T Experiments

All W/T experiments conducted within ADHeRo are performed in W/T A at the Technische Universität München in the Institute of Aerodynamics and Fluid Mechanics (TUM-AER). W/T A is a closed return type and can be operated either in an open or closed test section configuration. For **AD**HeRo, the test section is always operated in an open configuration, allowing a maximum free stream velocity U_∞ of 65 m/s. The standard freestream velocity for the **AD**HeRo measurements is 40 m/s. W/T A provides a freestream turbulence intensity below 0.4 % in all three directions in space. For this paper, no variations in angle of attack α and angle of sideslip β are considered. All results shown in this paper are recorded at α , β = 0°.

3.1 Aerodynamic Force Measurements

The aerodynamic forces and moments acting on the model are recorded with the six-component under-floor W/T balance. All recorded data are time-averaged. Preliminary testing revealed that the threshold value above which the results become independent of the integration time is 15 seconds. Thus this value is chosen for the aerodynamic force measurements performed. In this paper, all of the force data presented are made dimensionless. The resulting aerodynamic coefficients for drag C_D, side force C_Y and lift C_L are assessed through Eq. (3) to (5).

$$C_D = F_D / (½ \rho U_\infty^2 A_{ref}) \quad (3)$$

$$C_Y = F_Y / (½ \rho U_\infty^2 A_{ref}) \quad (4)$$

$$C_L = F_L / (½ \rho U_\infty^2 A_{ref}) \quad (5)$$

Note that the reference area A_{ref} is kept constant for all investigated configurations to facilitate the comparison of the respective aerodynamic coefficients.

3.2 Surface Pressure Measurements

In order to gather information about the local flow conditions on the surface of the model, the model is equipped with a pressure measurement system. The system incorporates a combination of steady and unsteady pressure sensors connected to pressure tabs at the model surface. Thus it is possible to record the local surface pressures at each of the pressure tabs during W/T runs. In total, 218 (192 steady and 26 transient) probing positions are equipped with sensors. Most of the measurement positions are clustered on the aft-body region, thus allowing a precise analysis of the flow around this region of the model. The remaining probing positions are distributed along the centerline and a horizontal section of the model. The sensor array on the W/T model is depicted in Fig. 1. In this paper, only time-averaged pressure distributions are presented. In accordance with the aerodynamic force measurements, the integration time is set to 15 seconds.

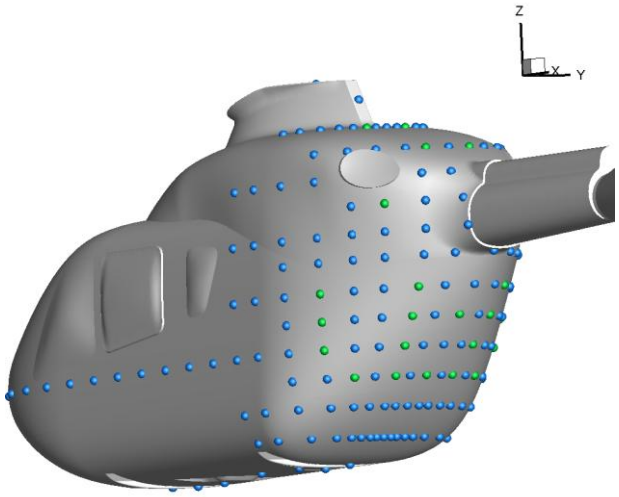

Fig. 4. Pressure probing positions. steady sensors (blue) and unsteady sensor (green).

3.3 Stereo Particle Image Velocimetry

Three-dimensional velocity field data is recorded in the wake of the W/T model through the application of Stereo Particle Image Velocimetry (Stereo-PIV) [5].

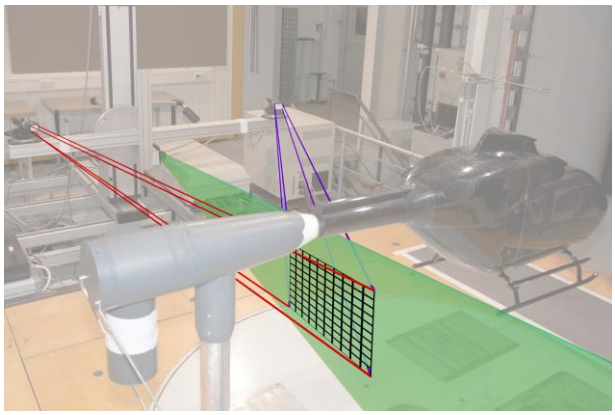

Fig. 5. Stereo PIV measurement setup.

For this purpose, particles are intermixed with the fluid. The technique is based on tracking the positions of these particles at two instances in time in quick succession. Their positions are tracked by illuminating the measuring plane with a laser sheet and capturing the light scattered back from the particles on camera. This allows computing displacement vectors for subsets of particles in the field of the camera's view between the two recorded events. In consequence, velocity vectors can be computed by dividing the displacements by the known time lag between the two events. Conventional PIV can only provide two-dimensional velocity vectors within the measuring plane.

The employed Stereo-PIV system allows recording the velocity components normal to the measuring plane by exploiting the principles of stereogrametry. The Stereo-PIV setup employed for **AD**HeRo is depicted in Fig. 5.

4 Numerical Method

In this section, the employed numerical method is described in detail. This includes the mesh generation process and the employed numerical setup for the different runs performed. Furthermore, the digital model geometry is presented and compared to the actual W/T model geometry.

4.1 Mesh Generation

The mesh generation is executed with the commercial meshing tool ANSYS ICEM CFD. The geometry investigated through numerical simulations is depicted in fig. 6. The digital helicopter model is of the same scale as the physical W/T model. Concerning the level of geometrical details, the digital model is almost identical to the W/T model. Only some minor modifications at the junction of the landing skids with the fuselage and at the rotor head were necessary to prepare the geometry for the meshing process. The horizontal conus of the model support is incorporated in the digital model, while the other parts are neglected. In analogy to the different configurations investigated through experiments, the flow is simulated for configurations F0M0, F0M0L0 and F0M0L0R0; see fig. 3.

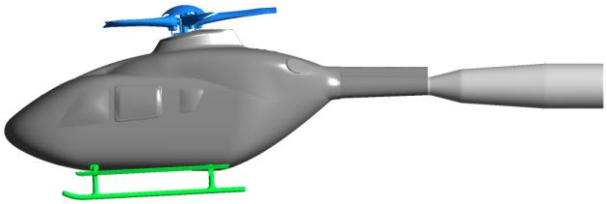

Fig. 6. Geometry used for numerical simulation of the W/T model flow.

In order to model the rotating rotor head, the computational domain is split into an inner and an outer part. The inner domain includes the rotor head, whereas the outer domain covers the fuselage with landing skids and the far field; see fig. 7.

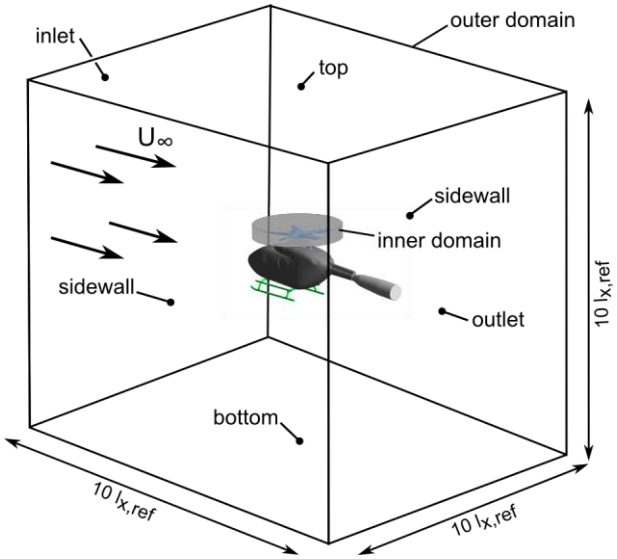

Fig. 7. Division of the computational domain into inner and outer domain.

Thus the rotation of the rotor head is simulated by defining a sliding mesh interface between the two domains. However, the cyclic pitch motion cannot be modeled with this approach.
For the actual meshing of the investigated configurations, unstructured meshes are chosen. The meshing is performed by applying the Octree method first to obtain the surface grids. Before computing the volume mesh with the Delauney algorithm, the surface grids are subjected to several smoothing loops. The obtained volume mesh is again smoothed before adding the prism layers. The prism layers, consisting of 21 single layers for our meshes, are generated near solid walls in order to finely resolve the regions of the flow where viscous effects dominate, i.e. the viscous sub-layer. This is achieved by confining the height of the prisms at the wall h_0, such that the equivalent dimensionless wall distance y^+ is less than one. A y+ value smaller than one is achieved for all employed grids. This circumvents the application of wall function to model viscous effects.

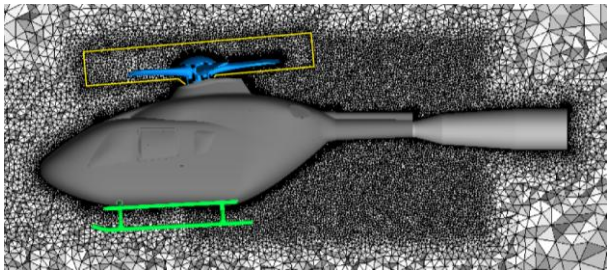

Fig. 8. Mesh topology in center plane near for configuration F0M0L0R0 including the domain interface (yellow).

This is crucial to the accuracy of numerical simulations for massively separated flows as observed on the configurations investigated here.
The final mesh in the vicinity of the model is depicted in Fig. 8 for configuration F0M0L0R0. Note that the grid in the wake of the model is additionally refined in order to capture the flow topology in the wake more precisely.

4.2 Solver Setup

All numerical results presented in this paper are obtained by solving the incompressible Navier Stokes equations through the application of the Reynolds Averaged Navier Stokes (RANS) equation model. Two types of simulations are performed, steady state and unsteady. For this purpose, the commercial solver ANSYS CFX 5 is used.
The type of run performed for each configuration is adapted such that the computational effort is minimal while the flow field topology is still captured with good precision. For configurations F0M0 and F0M0L0, it is therefore decided to perform steady-state simulations only. These runs are executed by employing the Explicit Algebraic Reynolds Stress Model (EARSM), based on the work of Launder et al. [6]. This modeling approach is numerically somewhat more expensive than the standard Shear Stress Transport (SST) model [7]. However, it is shown that employing the EARSM turbulence model makes it possible to perform steady-state simulations for configurations F0M0 and F0M0L0 without annihilating the validity of the solution. Thus, the total numerical effort is reduced with this approach.
For configuration F0M0L0R0, a steady-state simulation is not feasible, since the rotation of the rotor head can only be modeled through a time-accurate simulation. To confine the required additional numerical effort for the unsteady simulation, it is decided to employ the simpler SST turbulence model.
For the spatial discretization, a High Resolution Scheme is employed, blending between first and second-order accuracy. The temporal discretization is realized through the application of the implicit Backward – Euler – Method with second-order accuracy.

All steady-state simulations are performed by employing the automatic local timescale option provided through the solver. For the unsteady simulations, a physical time step of $8.7 \cdot 10^{-5}$ seconds is used. For details on the solver theory, please refer to [8].

Solving the set of differential equations also requires the definition of boundary conditions on the inlet, outlet, model surface, sidewalls, top and bottom of the computational domain; see Fig. 7. The boundary conditions for the simulation are imposed by defining

- the inflow with a constant velocity profile (turbulence intensity of 5%) at the inlet,
- the outflow with zero pressure gradient at the outlet
- no-slip walls at the surface of the model and
- free-slip walls at the sidewalls, the top and the bottom of the domain.

The steady-state simulation runs are initialized by imposing the inlet conditions on the entire computational domain. For the unsteady run, the computational domain is initialized by importing the results of a fully converged steady-state RANS simulation performed in advance.

5 Experimental Results

In this section we present the results obtained during the baseline-model W/T campaign. First of all, the aerodynamic force measurements are analyzed. This includes the analysis of the drag factions of configuration F0M0L0R0 as well as configuration studies. Second, the surface pressure distributions obtained through pressure probing are analyzed. This sets the focus on substantiating the trends observed for the aerodynamic forces. Finally, the velocity field data in the wake of configuration F0M0 and F0M0L0 are compared against each other.

5.1 Aerodynamic Forces

Fig. 9 depicts the drag breakdown for the configuration F0M0L0R0 with rotating rotor head, trimmed for fast level flight. The drag fraction of the rotor head $F_{D,R0}$, the landing skids $F_{D,L0}$ and the fuselage $F_{D,F0M0}$ are assessed through Eq. (7) – (9). These equations are based on the measured drag of configurations F0M0, F0M0L0, F0M0R0 and F0M0L0R0. All miscellaneous drag fractions $F_{D,Misc}$ are united by applying Eq. (10).

$$F_{D,R0} = F_{D,F0M0L0R0} - F_{D,F0M0L0} \quad (7)$$

$$F_{D,L0} = F_{D,F0M0L0R0} - F_{D,F0M0R0} \quad (8)$$

$$F_{D,F0M0} = F_{D,F0M0} \quad (9)$$

$$F_{D,Misc} = F_{D,F0M0L0R0} - F_{D,R0} - F_{D,L0} - F_{D,F0M0} \quad (10)$$

The reference for the percentages given in fig. 9 is $F_{D,F0M0L0R0}$.

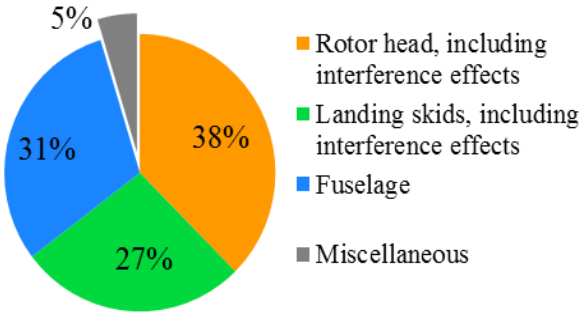

Fig. 9. Drag breakdown for configuration F0M0L0R0, α, β = 0°

The drag breakdown for the **AD**HeRo W/T model reveals that the rotor head together with the landing skids accounts for some 65 % of the parasite drag. This amount is slightly higher compared to the values found in literature; see Fig. 1. However, keep in mind that the tailboom is truncated upstream of the stabilizers for the **AD**HeRo W/T model. In consequence, the drag of these components is missing in the drag composition, leading to slightly different trends. Additionally, the drag assessed for the rotor head $F_{D,R0}$ and the landing skid $F_{D,L0}$ also includes the interference drag on other model components. For the rotor head, this includes the interference drag on the fuselage and on the landing skids, for example. This is due to the fact that no forces and moments could be recorded separately for these two components. Table 2 lists the drag coefficient C_D and lift coefficients C_L for configurations F0M0, F0M0L0, F0M0R0 and F0M0L0R0.

For configuration F0M0L0R0, both the results with and without ($\Psi = 0°$) rotation of the rotor head are shown. By comparing the lift coefficients of the configurations F0M0 and F0M0L0, we can identify a strong impact of the landing skid on the down force.

Configuration	C_D	C_L
F0M0	0.09053	- 0.08351
F0M0L0	0.18103	- 0.01360
F0M0R0	0.21639	- 0.03694
F0M0L0R0 ($\Psi = 0°$)	0.31541	- 0.00160
F0M0L0R0	0.30205	0.04555

Table 2. Aerodynamic drag, side force and lift coefficient for the different configurations experimentally investigated, $\alpha, \beta = 0°$.

However, the base and the step of the landing skids are inclined by 3 degrees pitch down relative to the freestream direction. Thus the landing skids alone would rather increase the down force instead. Furthermore, the drag coefficient doubles by adding the landing skids to the configuration F0M0. It seems unlikely that only the drag on the landing skids causes this increase in drag. Apparently the flow perturbations in the wake of the landing skids lead to a premature flow separation on the rear fuselage upsweep. This explains both of the effects. On one hand, extending the size of the separation region reduces the pressure recovery in the affected region, leading to higher drag. On the other hand, this deficit in pressure recovery reduces the down force in consequence of a reduced pressure difference between the upper and lower half of the fuselage. This aspect is addressed again in section 5.2 by analyzing the surface pressure distribution on the rear fuselage upsweep.

Studying the difference in lift coefficient between configuration F0M0R0 and F0M0 reveals that the presence of the rotor head reduces the down force. Comparing the lift coefficient of configuration F0M0L0R0 with and without rotation of the rotor head shows a clear increase in lift in consequence of the rotation of the rotor. Thus it is evident that the rotor generates vertical thrust even though the blade cuffs are cut off at the first aerodynamic section of the blade in the radial direction. However, the additional lift is probably not only associated with the rotor thrust. In consequence of the rotor thrust, a downwash is generated, which interacts with the flow over the upper fuselage. This changes the pressure distribution in this region, leading to a different lift coefficient.

The comparison of the drag coefficients of configuration F0M0L0R0 and F0M0L0R0 ($\Psi = 0°$) shows that the rotor generates not only vertical thrust but also axial thrust in the direction of flight. Thus the drag for configuration F0M0L0R0 recorded through the W/T balance is lower than without the rotation. Hence, even with the relatively short blade cuffs incorporated on the **AD**HeRo W/T model, the effect of thrust vectoring through the cyclic pitch input is observed. Leishman [9] presents a more thorough description of this matter.

Furthermore, it is found that the configuration F0M0L0R0 ($\Psi = 0°$) generates less down force than the configuration F0M0L0. Besides the interference effect of the non-rotating rotor head on the flow over the fuselage, another effect is responsible for this influence. Studying the geometry of the rotor head (Fig. 2) shows that the hub cap shape features a positive curvature on which lift is generated. Vogel et al. [10] proofed this effect both through experiments and numerical simulations for a slightly different rotor head geometry. Based on the experimental data obtained in the course of this work, it is not possible to differentiate the influence of the hub cap. Therefore, this matter is addressed again in the analysis of the numerical results; see section 6.

5.2 Surface Pressure Distributions

In Fig. 10, the measured surface pressures for three configurations (F0M0, F0M0L0, F0M0L0R0) are depicted as contour plots of local pressure coefficient C_P. For this purpose the pressure coefficients at each sensor position are interpolated via a kriging function on the rear surface of the W/T model.

For the configuration F0M0, the pressure recovers up to one-third of the stagnation pressure on the rear fuselage upsweep; see Fig. 10 a). That is the highest pressure recovery observed in this region on all three configurations. This can explain the relatively low drag coefficient measured for configuration F0M0; see Table 2. Thus, the flow is attached to the surface contour of the rear fuselage upsweep long enough to result in a comparatively strong upward deflection of the flow; see section 5.3. This is the reason why the highest negative lift coefficient is recorded on the isolated fuselage.

In the presence of the landing skids, the surface pressure distribution on the rear fuselage upsweep alternates considerably; see Fig. 10 b).

It can be observed that the region of high pressure coefficients is remarkably reduced. Furthermore, the highest overpressure achieved is reduced to $C_P \approx 0.2$. This reveals that the flow perturbations originating from the landing skids induce a premature flow separation on the flow past the rear fuselage upsweep, thereby explaining both the increase in drag and the reduction of down force in the presence of the landing skids.

Comparing the surface pressure distribution of configuration F0M0L0R0 against the corresponding distribution for configuration F0M0L0 shows the impact of the rotor downwash on the flow around the rear fuselage. The first difference observed is that the maximum overpressure is reduced compared to configuration F0M0L0. The maximum is now $C_P \approx 0.15$. In addition to this reduction, the extension of the region of maximum overpressure is smaller. However, the region of intermediate overpressures apparently increases compared to the configuration without the rotor head. In particular, the overpressure increases in the region of the rear fuselage upsweep. Thus the interference of the rotor downwash with the flow over the fuselage as emphasized earlier can actually be confirmed. Its characteristic is somewhat different than expected. Instead of only affecting the pressure distribution on the upper fuselage, its impact also extends to the rear fuselage upsweep. Overall, this interference leads to an increase in lift generated at the fuselage, by increasing the pressure on the lower half and reducing it on the upper half of the fuselage.

5.3 Particle Image Velocimetry

The effect of the landing skid on the wake flow of the model is investigated through axial velocity contours in a plane downstream of configuration F0M0 and F0M0L0, depicted in Fig. 11. In-plane velocity components are superimposed as vector symbols. The data are recorded with the Stereo-PIV setup presented in section 3.2. The location of the measuring plane is highlighted in the small box on the left of fig. 11 a) and b).

It can be observed that the region of axial velocity deficit ($U / U_\infty < 1$) increases by attaching the landing skids. Thus the velocity field data supports the indications observed in the aerodynamic forces and surface pressure data for an impact of the landing skid on the flow separation over the rear fuselage upsweep. However, by analyzing the shape of the region of axial velocity deficit, Fig. 11 b), two bulges in lateral symmetry to the center plane can be identified. These bulges are not associated with the separation on the rear fuselage upsweep, but with the wake of the landing skids.

Comparing the in-plane velocity components in the wake behind the fuselage with and without the landing skids confirms another supposition. That is the impact of the landing skids on the deflection of the flow at the fuselage. In Fig. 11 a), a strong upward deflection of the flow is evident near the symmetry plane behind the rear fuselage upsweep. In the presence of the landing skids, this upward deflection is reduced significantly; see fig. 11 b). Thus it can be proved that the landing skids reduce the down force generated at the fuselage by disturbing the upward deflection of the flow around the rear fuselage upsweep.

Another flow phenomenon is observed in the velocity field measured in the wake behind the mast fairing. Both in Fig. 11 a) and b), two comparatively strong counter-rotating vortices can be identified. The source of this vortex pair cannot be identified through the experimental data. Therefore this aspect is addressed again in the analysis of the numerical results in section 6.

6 Numerical Simulations

Before analyzing the flow characteristics based on the numerical simulations, the results are verified against experimental data. This is performed by comparing the drag and lift coefficient obtained both through experiments and numerical simulations for configurations F0M0, F0M0L0 and F0M0L0R0 without cyclic pitch input ($\alpha_{cyclic} = 0°$).

Configuration	$C_{D,exp}$	$C_{D,sim}$	$C_{L,exp}$	$C_{L,sim}$
F0M0	0.0905	0.0837	- 0.0835	- 0.0940
F0M0L0	0.1810	0.1778	- 0.0136	0.0072
F0M0L0R0 ($\alpha_{cyclic} = 0°$)	0.3023	0.3167	0.2235	0.2111

Table 3. Comparison of numerical and experimental results for drag and lift coefficients.

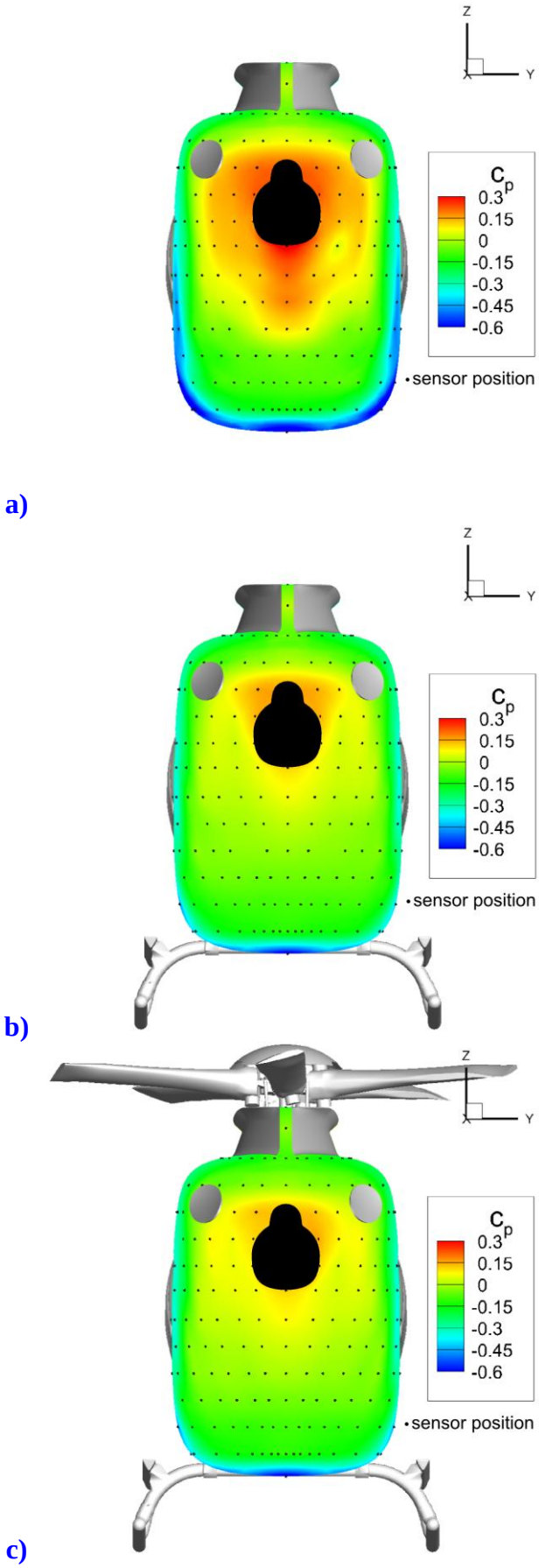

Fig. 10. Measured surface pressure distribution interpolated on rear fuselage surface for configurations a) F0M0, b) F0M0L0 and c) F0M0L0R0 at α, β = 0°.

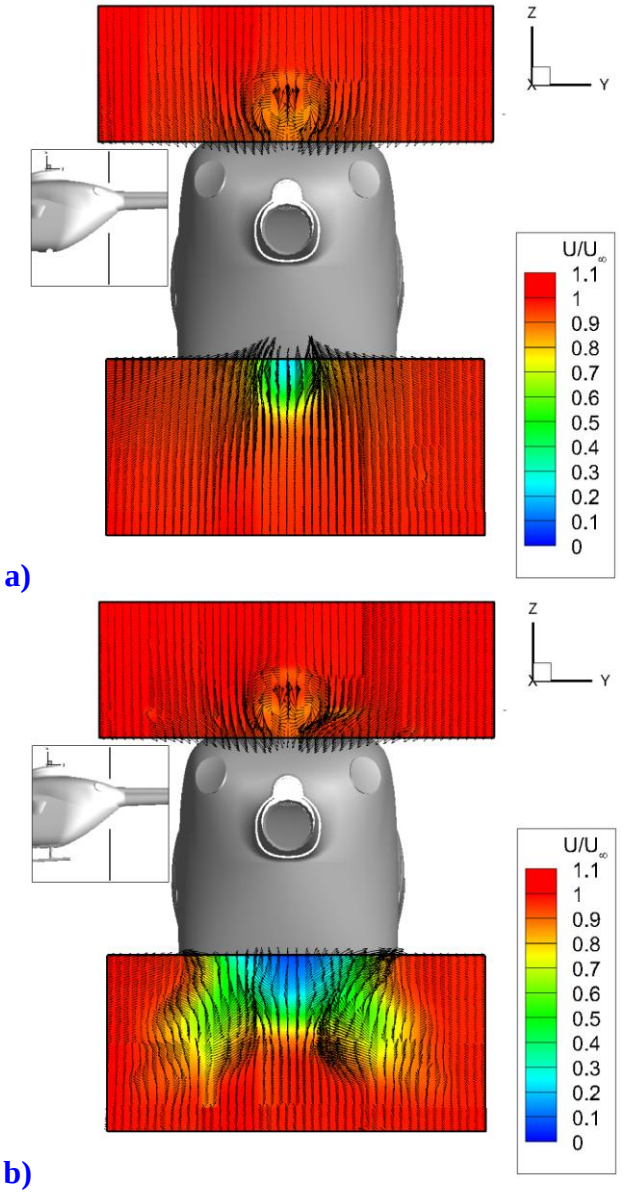

Fig. 11. Axial velocities in two PIV planes downstream from the model superimposed with in-plane velocity vectors for configuration a) F0M0 and b) F0M0L0 at α, β = 0°.

The correspondent values of drag and lift coefficient are listed in Table 3. The comparison of the measured drag coefficients $C_{D,exp}$ against drag coefficients predicted through numerical simulations $C_{D,sim}$ shows a good agreement for all configurations. The relative deviation of the numerical results is well below 10 % in all three cases. Repeating this analysis for the lift coefficients reveals slightly different trends. By comparing the experimental and numerical results for the lift coefficient of configuration F0M0, a slight over-prediction of the down force generated at the fuselage through the simulation can be identified.

The observed deviation is about 13%. For configuration F0M0L0, the simulation predicts a modest lift, whereas a small down force is identified in the experiment. Even though the resulting relative deviation is large, this deviation is agreeable since the absolute difference is small. The lift generated on configuration F0M0L0 is predicted very well, confining the relative deviation of the numerical results to some 6 %. Hence, it is concluded that the flow topology for the investigated configurations is predicted well by the numerical simulations. Therefore the numerical results are employed in the following analysis to supplement the study based on experimental data performed earlier.

Fig. 12 depicts the drag breakdown for configuration F0M0L0R0 calculated from numerical data. The stated drag fractions are given in percentage of the total drag of configuration F0M0L0R0, corrected for the axial thrust of the rotor head. The thrust generated at the rotor head is assessed by comparing the drag of the rotor head with and without rotation of the rotor head. Comparing the drag fractions assessed from numerical data with the ones based on the experimental results, different trends can be observed. However, it is still possible to derive valuable information from this analysis. The results depicted in Fig. 12 provide further evidence that additional drag observed in the presence of the landing skids is caused through the interference drag on the fuselage.

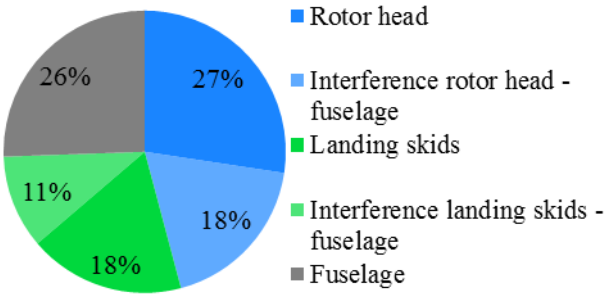

Fig. 12. Drag breakdown for configuration F0M0L0R0 calculated from numerical data, α, β = 0°.

Additionally, it can be seen that the additional drag caused by the rotor head is mainly generated at the rotor head itself. Interference effects of the rotor head on other model components are also considerable.

Fig. 13 shows the lift coefficients of the different rotor head components for configuration F0M0L0R0.

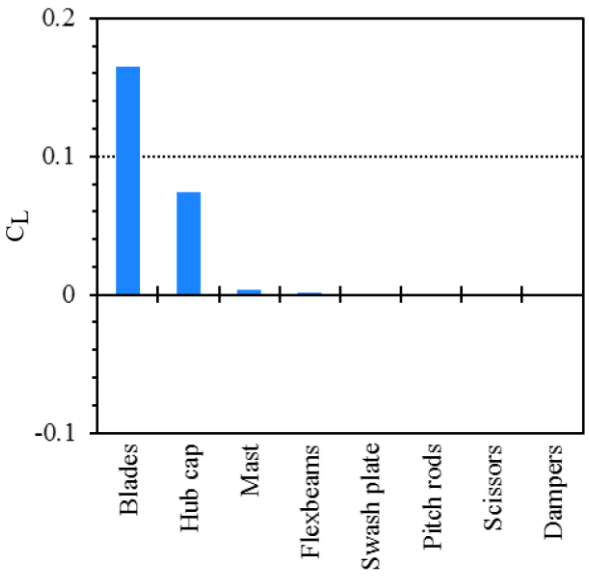

Fig. 13. Lift fractions of rotor head components for configuration F0M0L0R0, α, β = 0°.

It is apparent that in addition to the blade cuffs, the hub cap considerably contributes to the lift generated on the rotor head. This confirms the hub cap contribution to the lift generation already mentioned in section 5.1. None of the other rotor head components significantly affect the lift.

Fig. 14 depicts the average flow conditions at the rear fuselage of configurations F0M0, F0M0L0 and F0M0L0R0. In analogy to Fig. 10, the surface pressure distributions are depicted as contour plots. Additionally, the surface stream lines computed from the simulations are superimposed over the pressure contours. The results of the unsteady simulation of configuration F0M0L0R0 are averaged over one rotor head cycle for the visualization presented in Fig. 14 c).

Fig. 15 shows the vortex structures in the wake of the model for the steady-state simulations of the flow around configuration F0M0 and F0M0L0. To visualize the coherent vortex structures in the wake of the model, the iso-surfaces of the Q-Criterion are computed. A detailed description of the theoretical background of the Q-Criterion is presented by Dubief and Delcayre [11]. The sense of rotation of these vortex structures is illustrated by coloring the respective iso-surfaces with the non-dimensional local axial vorticity contours.

The vorticity is defined such that positive values indicate a rotation in the mathematical positive sense around the x-axis.

Analyzing the surface streamlines in Fig. 14 c) reveals that the flow past the rear fuselage upsweep of configuration F0M0 mainly stays attached near the symmetry plane of the model. This also explains the high pressure recovery already observed in the experimental pressure data, see fig. 10 a). On the side of the fuselage upsweep, it is observed that the surface streamlines converge towards a line following an S-shaped path. This normally indicates the formation of a strong vortex tube in the affected region. Studying the coherent structures in the wake of this configuration, see fig. 15 a), actually confirms the existence of this vortex tube. It can be observed that a similar vortex tube is generated at the averted side of the model.

These two vortex tubes are shed into the wake, forming a pair of counter-rotating vortices below the tailboom. As a result of the described vortex tubes, the flow is accelerated near the walls in consequence of the rotation. This leads to a region of lower surface pressures, thereby also explaining the dents in the region of maximum overpressures in Fig. 10 a) on both sides of the symmetry plane.

Another, less dominant vortex pair is identified, which originates in the region just downstream from the closed ejectors. Studying the surface streamline pattern reveals that the flow coming past the upper half of the fuselage interacts with the flow past the rear fuselage upsweep in this region. This leads to the observed roll-up of the counter-rotating vortex pair.

Comparing the flow topology of configuration F0M0 with the one observed for configuration F0M0L0 shows a strong impact by the landing skids. Studying the surface streamline pattern in Fig. 14 b) reveals a pronounced recirculation zone spanning the entire central region of the rear fuselage upsweep.

The breakdown of the attached flow over this region leads to a considerable change in the flow field topology in the presence of the landing skids. The flow over the upper half of the fuselage now impinges down into the rear fuselage upsweep. In consequence, the two vortex tubes originating from the side of the rear fuselage upsweep diminish. However, the impingement of the upper fuselage flow leads to the roll-up of a new pair of vortex tubes. These vortex tubes originate at each side of the tailboom junction; see Fig. 15 b). As for the vortex tubes observed without the landing skids, the vortex tubes in the presence of the landing skids form a counter-rotating vortex pair below the tailboom. However, the sense of rotation of this new pair of counter rotating vortices is inverted compared to the one observed without the landing skids.

In the analysis of the velocity fields measured with the Stereo-PIV system, a pair of counter-rotating vortices is detected in the wake behind the upper half of the fuselage. This vortex pair is also present in the numerical simulations of the flow past configurations F0M0 and F0M0L0. Analyzing the coherent structures visualized through the Q-Criterion in Fig. 15 a) and b) reveals that this vortex pair actually originates at the rear side of the mast fairing.

Finally, the flow topology on the rear part of the fuselage of configuration F0M0LOR0 with a rotating rotor head is analyzed. Studying the drag breakdown calculated from the numerical data shows a considerable interference drag on the fuselage by adding the rotating rotor head. Comparing the surface flow pattern in the aft-body region with and without the rotor head, depicted in Fig. 14 b) and c), no clear trend to supports this fact are observed. It can be seen that the extension of the recirculation zone is not affected considerably by the wake and the downwash of the rotor head. However, the flow topology within the recirculation zone changes considerably. Note that this change might also result from averaging the flow field over one rotor cyclic. To identify the actual source of the strong interference drag caused by the rotor head further analysis is to be performed. The two vortices already observed on configuration F0M0L0 at the side of the tailboom junction are still present.

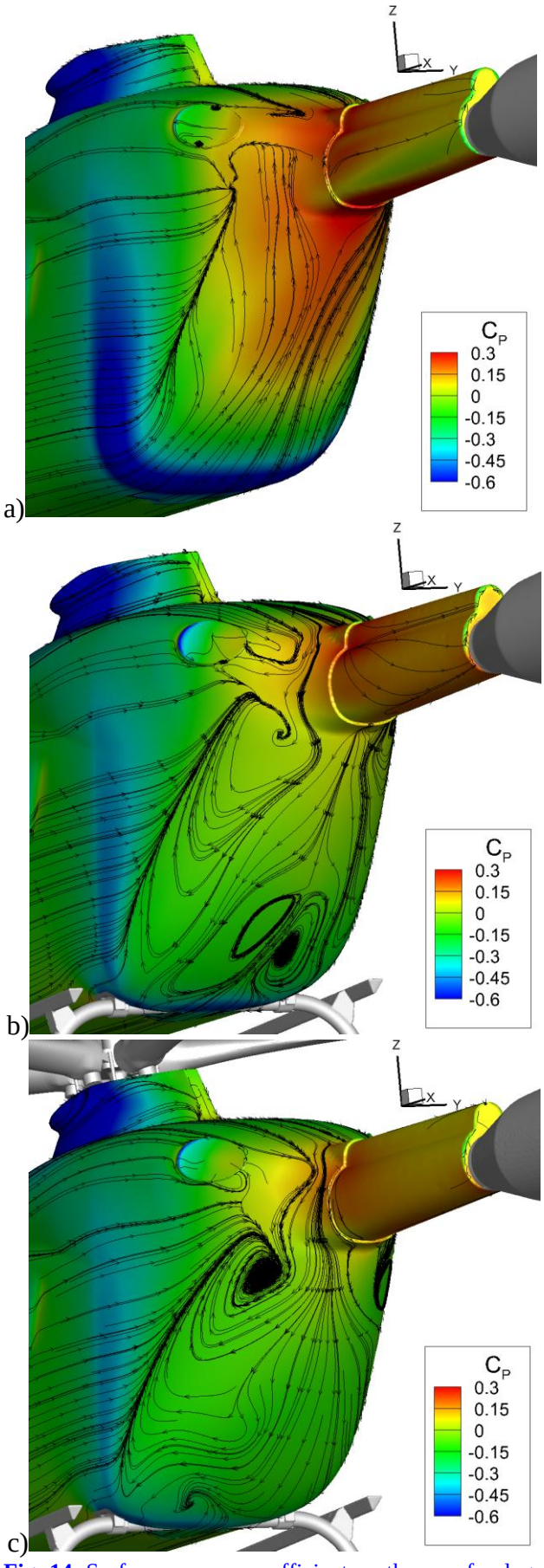

Fig. 14. Surface pressure coefficient on the rear fuselage of configurations a) F0M0, b) F0M0L0 and c) F0M0L0R0 superimposed with surface stream lines.

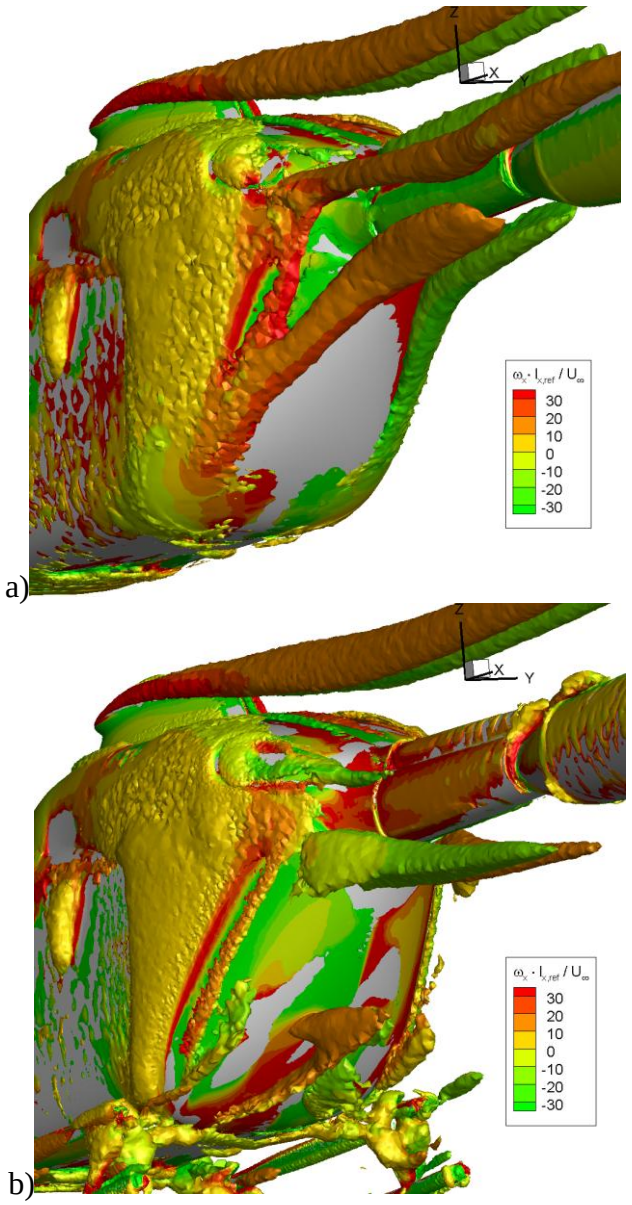

Fig. 15. Wake flow of configurations a) F0M0 and b) F0M0L0, visualized by iso - surfaces of the Q-Criterion colored with the local axial vorticity.

7 Conclusions and Outlook

In the framework of the CleanSky Joint Technology Initiative, the GRC subproject **AD**HeRo was initiated in order to increase the aerodynamic efficiency of light-weight rotorcraft. This paper reported on the **AD**HeRo baseline model campaign, which was conducted to provide reference data and identify potentials for upcoming optimization tasks on a Twin Engine Light (TEL)-class utility helicopter. The baseline campaign has provided valuable data both through wind tunnel experiments and numerical simulations. Based on the obtained data set, a detailed study of both global and local flow parameters has been performed.

The presented analysis has placed a special focus on configuration studies. As a result, a better understanding of the main contributors to the parasite drag and lift of TEL-class helicopter could be gained. It was shown that for the investigated configuration the landing skids and the rotating rotor head account for 65 % of the total parasite drag. Furthermore, it was revealed that a significant part of the parasite drag caused by the landing skids arises from the interference drag on the rear fuselage upsweep. We showed that this interference drag results from an extension of the separation region on the rear fuselage, which is caused through the flow perturbation in the wake of the landing skids. The interference of the rotor head wake with the fuselage also causes significant interference drag. In addition, the importance of taking the lift characteristics into consideration for the planned optimization was shown.

Based on the work performed, it becomes clear that reducing the drag of the investigated configuration is best achieved by reducing the drag of the landing skids and the rotor head, and by attenuating the interference effects associated to these two components. Furthermore, means to confine an increase in down force were identified, such as the lift-producing hub cap. This constitutes the basis for the upcoming optimization tasks and will be accounted for in the design process of the modified components.

8 Acknowledgments

The research leading to these results received funding from the European Community's Seventh Framework Program (FP/2007-2013) for the Clean Sky Joint Technology Initiative under grant agreement number 270563.

The authors would like to thank project partner Eurocopter Deutschland GmbH for the fruitful collaboration and valuable support.

Furthermore, special thanks are addressed to ANSYS CFX for providing the flow simulation software.

The work of our students Ziga Babosek, Victor Stein and Matthias Tebbe is also highly appreciated.

References

[1] Private communication with Eurocopter Deutschland GmbH

[2] Stroub R H and Rabbott J P Jr. Wasted Fuel – Another Reason for Drag Reduction, *31st Annual National Forum of the American Helicopter Society*, Washington, D.C., May 1975

[3] Wagner, S N. Problems of Estimating the Drag of a Helicopter, *AGARD Conference Proceedings No. 124*, April, 1973

[4] Vogel F, Breitsamter C and Adams N A. Aerodynamic Investigations on a Helicopter Fuselage, *Proceedings of the 29th AIAA Applied Aerodynamics Conference*, Honolulu, HI 2011.

[5] Raffel M, Willert C E, Wereley S T and Kompenhans J. *Particle Image Velocimetry - A Practical Guide*, 2nd edition, Springer, 2007

[6] Launder B E, Reece G J and Rodi W. Progress in the development of a Reynolds-stress turbulence closure. *Journal of Fluid Mechanics*, Vol. 68, No. 3, pp. 537-566, 1975

[7] Menter F R. Zonal two-equation k-ω turbulence model for aerodynamic flows. *AIAA Journal*, Vol. 32, No. 8, pp. 1598-1605, 1994.

[8] ANSYS, Inc., *CFX – Solver Theory Guide Release 13.0*, 2010

[9] Leishman J G. *Principles of Helicopter Aerodynamics*, 2nd edition, p. 202 f, Cambridge University Press, 2006.

[10] Vogel F, Breitsamter C and Adams N A. Aerodynamic Investigations on a Helicopter Main Rotor Hub, *Proceedings of the American Helicopter Societies 66th Annual Forum*, Phoenix, AZ, 2010.

[11] Dubief Y, Delcayre F. On coherent-vortex identification in turbulence. *Journal of Turbulence*, Vol. 1, pp. 1 – 22, 2000.

Copyright Statement

The authors confirm that they, and/or their company or organization, hold copyright on all of the original material included in this paper. The authors also confirm that they have obtained permission, from the copyright holder of any third party material included in this paper, to publish it as part of their paper. The authors confirm that they give permission, or have obtained permission from the copyright holder of this paper, for the publication and distribution of this paper as part of the ICAS2012 proceedings or as individual off-prints from the proceedings.